Vol 17 No 3, March 2008
1674-1056/2008/17(03)/1078-06
Chinese Physics B
© 2008 Chin. Phys. Soc.
and IOP Publishing Ltd

Phase-field simulation of dendritic growth in a binary alloy with thermodynamics data*

Long Wen-Yuan(龙文元), Xia Chun(夏 春),
Xiong Bo-Wen(熊博文), and Fang Li-Gao(方立高)

College of Material Science and Engineering, Nanchang Hangkong University, Nanchang 330063, China

(Received 5 February 2007; revised manuscript received 20 September 2007)

This paper simulates the dendrite growth process during non-isothermal solidification in the Al–Cu binary alloy by using the phase-field model. The heat transfer equation is solved simultaneously. The thermodynamic and kinetic parameters are directly obtained from existing database by using the Calculation of Phase Diagram (CALPHAD) method. The effects of the latent heat and undercooling on the dendrite growth, solute and temperature profile during the solidification of binary alloy are investigated. The results indicate that the dendrite growing morphologies could be simulated realistically by linking the phase-field method to CALPHAD. The secondary arms of solidification dendritic are better developed with the increase of undercooling. Correspondingly, the tip speed and the solute segregation in solid–liquid interface increase, but the tip radius decreases.

Keywords: phase-field model, dendritic growth, CALPHAD, binary alloy
PACC: 6410, 6155H, 6100, 8130

1. Introduction

Phase-field simulations have attracted considerable interest in the last decade as a means of simulating dendritic growth in solidification. The model was originally applied for simulating dendritic growth in the undercooled melt of pure material.[1−4] Now the model has been extended to the solidification of alloys. The first phase-field model for alloys was developed by Wheeler, Boettinger and McFadden[5] (WBM model) in a thermodynamically consistent way. The WBM model has been most widely used.[5,6] In this model, the mixture of solid and liquid both with a same composition is assumed in the interface region.

Recently, Kim S G, Kim W T and Suzuki T[7] have proposed a new phase-field model for binary alloys (KKS model). The model is equivalent to the WBM model, but it has a different definition of the free energy density for the interfacial region. The limit of the interface width in the WBM model disappears. The model has been used by the original authors to study microstructure evolution during the rapid solidification of Fe–C, Fe–C–P and Al–Cu alloys.[7,8] Now the phase-field models have become very popular for the simulation of microstructure evolution during solidification process.[9−14]

In the present paper, we attempt to simulate the dendritic growth during solidification in the Al–Cu binary alloys by linking the phase-field model to Calculation of Phase Diagram (CALPHAD). The thermodynamic data for the Al–Cu binary alloy is obtained by using the CALPHAD approach.

2. Governing equations

In the phase-field model, the state of the phase is represented continuously by an order parameter, the phase-field, ϕ. For example, ϕ=1, ϕ=0 and a finite region in which $0 < \phi < 1$ represent solid, liquid and the interface respectively. For a binary alloy, the detailed equation of the phase-field is given as[14]

$$\frac{1}{M}\frac{\partial \phi}{\partial t} = \varepsilon^2 \nabla^2 \phi - \frac{RT}{V_{\mathrm{m}}} h'(\phi) \left[c \ln \frac{c_{\mathrm{S}} c_{\mathrm{L}}^{\mathrm{e}}}{c_{\mathrm{L}} c_{\mathrm{S}}^{\mathrm{e}}} + (1-c) \ln \frac{(1-c_{\mathrm{S}})(1-c_{\mathrm{L}}^{\mathrm{e}})}{(1-c_{\mathrm{L}})(1-c_{\mathrm{S}}^{\mathrm{e}})} \right] - W g'(\phi), \tag{1}$$

*Project supported by Research Center of Material Science and Engineering of Jiangxi Province, China (Grant No ZX200301017).

$$\frac{\partial c}{\partial t} = \nabla \cdot \left\{ D(\phi)c(1-c)\left[(h(\phi)\frac{1}{c_{\mathrm{S}}(1-c_{\mathrm{S}})} + (1-h(\phi))\frac{1}{c_{\mathrm{L}}(1-c_{\mathrm{L}})} \right] \nabla c \right. \\ \left. - D(\phi)c(1-c)h'(\phi)\left[\ln\frac{(1-c_{\mathrm{L}}^{\mathrm{e}})c_{\mathrm{S}}^{\mathrm{e}}}{(1-c_{\mathrm{S}}^{\mathrm{e}})c_{\mathrm{L}}^{\mathrm{e}}} + \ln\frac{(1-c_{\mathrm{S}})c_{\mathrm{L}}}{(1-c_{\mathrm{L}})c_{\mathrm{S}}} \right] \nabla\phi \right\}, \quad (2)$$

where M is the phase-field mobility which is related to the driving force for the interface, R is the gas constant, T is temperature, c is the solute composition, the superscript e represents equilibrium state, the subscripts S and L represent solid and liquid phases respectively, V_{m} is the molar volume, ε is the phase-field parameter, $h(\phi)$ is the potential function $h(\phi) = \phi^3(10 - 15\phi + 6\phi^2)$, $g(\phi)$ is the double-well potential $g(\phi) = \phi^2(1-\phi)^2$, W is the height of the double-well potential, $D(\phi)$ is solute diffusion coefficient $D(\phi) = D_{\mathrm{L}} + h(\phi)(D_{\mathrm{S}} - D_{\mathrm{L}})$, D_{S} and D_{L} are the diffusivities in the solid and liquid respectively.

The solute composition in the interface region is the fraction-weighted sum of solid and liquid compositions. The chemical potentials of solute and solvent are selected as a thermodynamic variable of constraint, and those of solid and liquid phases are assumed to be equal at any point within the interface region, i.e.

$$c = h(\phi)c_{\mathrm{S}} + (1 - h(\phi))c_{\mathrm{L}}, \quad (3)$$

$$\mu^{\mathrm{S}}(c_{\mathrm{S}}(x,t)) = \mu^{\mathrm{L}}(c_{\mathrm{L}}(x,t)). \quad (4)$$

The latent heat extraction is estimated by summing up the change of phase-field within the corresponding temperature grid, then the thermal diffusion equation is obtained as follows:

$$\frac{\partial T}{\partial t} = D_{\mathrm{T}}\nabla^2 T + \frac{L}{c_{\mathrm{p}}}\sum Ah'(\phi)\frac{\partial\phi}{\partial t}, \quad (5)$$

where D_{T} is thermal diffusivity of the alloy, L is the latent heat per unit volume, c_{p} is specific heat and A represents the area ratio of the phase-field grid to the thermal one.

3. Phase-field parameters

The phase-field parameter of ε and W are related to the interface energy, σ, and the interface width, 2λ. From the definition of interface energy and interface thickness, ε and W can be determined.

$$\sigma = \frac{\varepsilon\sqrt{W}}{3\sqrt{2}}, \quad 2\lambda = 2.2\sqrt{2}\frac{\varepsilon}{\sqrt{W}}. \quad (6)$$

The phase-field mobility M is related to the interface kinetic coefficient, β. It can be obtained from the fact that the thin-thickness is small compared with the diffusive boundary layer as follows:[13]

$$M^{-1} = \frac{\varepsilon^2}{\sigma}\left[\frac{RT}{V_{\mathrm{m}}}\frac{1-k_{\mathrm{e}}}{m_{\mathrm{e}}}\beta + \frac{\varepsilon}{D_{\mathrm{i}}\sqrt{2W}}\zeta(c_{\mathrm{S}}^{\mathrm{e}}, c_{\mathrm{L}}^{\mathrm{e}}) \right], \quad (7)$$

$$\zeta(c_{\mathrm{S}}^{\mathrm{e}}, c_{\mathrm{L}}^{\mathrm{e}}) = \frac{RT}{V_{\mathrm{m}}}(c_{\mathrm{L}}^{\mathrm{e}} - c_{\mathrm{S}}^{\mathrm{e}})\int_0^1 \frac{h(\phi)(1-h(\phi))}{(1-h(\phi))c_{\mathrm{L}}^{\mathrm{e}}(1-c_{\mathrm{L}}^{\mathrm{e}}) + h(\phi)c_{\mathrm{S}}^{\mathrm{e}}(1-c_{\mathrm{S}}^{\mathrm{e}})} \cdot \frac{\mathrm{d}\phi}{\phi(1-\phi)}, \quad (8)$$

where m_{e} is equilibrium slope of the liquidus, k_{e} is the equilibrium partition coefficient, and D_{i} is the diffusion coefficient in the interface region.

4. Calculations

4.1. Thermodynamic data

Usually the thermodynamic data is obtained from the phase diagram, the absence of the phase diagram data will restrict the development of the phase-field. Reference [15] initially attempted to develop a 3D phase-field model for modelling the microstructure evolution in Ni-base superalloys, the local free energy as a function of composition and order parameters is directly constructed by using the CALPHAD method and thus relies on existing thermodynamic databases to supply the necessary thermodynamic input.

In this paper, we attempt to link the phase-field model to CALPHAD. The thermodynamics data for the Al–Cu binary alloy is obtained by using the CALPHAD approach. The liquid and fcc phases are mod-

elled as substitutional solutions by assuming random mixing of Al and Cu atoms and therefore no short-range order is considered. Using a Redlich–Kister polynomial to describe the excess Gibbs energy of mixing, we can write the total Gibbs energy as[16]

$$\begin{aligned} G_{\mathrm{m}}^{\phi} =& x_{\mathrm{Al}}{}^{0}G_{\mathrm{Al}}^{\phi} + x_{\mathrm{Cu}}{}^{0}G_{\mathrm{Cu}}^{\phi} \\ &+ RT(x_{\mathrm{Al}}\ln x_{\mathrm{Al}} + x_{\mathrm{Cu}}\ln x_{\mathrm{Cu}}) \\ &+ x_{\mathrm{Al}}x_{\mathrm{Cu}}\sum_{k=0}^{n}{}^{k}L_{\mathrm{Al,Cu}}^{\phi}(x_{\mathrm{Al}}-x_{\mathrm{Cu}})^{k}, \end{aligned} \quad (9)$$

where x_i is the composition of element i in structure ϕ, ${}^{0}G_{\mathrm{i}}^{\phi}$ is the molar Gibbs energy of pure element i in structure ϕ, taken from the Scientific Group Thermodata Europe (SGTE) pure element database.[17] ${}^{k}L_{\mathrm{Al,Cu}}^{\phi}$ is the kth interaction parameter between the Al and Cu atoms. The Gibbs energy parameters for the liquid and fcc are listed in Table 1. The phase diagram of Al–Cu alloys is calculated by Thermo-Calc.[18]

Table 1. Thermodynamic parameters of the Al–Cu system.[16]

liquid: (Al, Cu)
${}^{0}L_{\mathrm{Al,Cu}}^{\mathrm{liq}} = -66622 + 8.1T$, ${}^{1}L_{\mathrm{Al,Cu}}^{\mathrm{liq}} = 46800 - 90.8T + 10T\ln T$, ${}^{2}L_{\mathrm{Al,Cu}}^{\mathrm{liq}} = -2812$
Fcc: (Al, Cu)
${}^{0}L_{\mathrm{Al,Cu}}^{\mathrm{fcc}} = -53520 + 2T$, ${}^{1}L_{\mathrm{Al,Cu}}^{\mathrm{fcc}} = 38590 - 2T$, ${}^{2}L_{\mathrm{Al,Cu}}^{\mathrm{fcc}} = 1170$

4.2. Finite difference techniques

In the calculation, Eqs.(1) and (2) were discretized on uniform grids by using an explicit finite difference scheme. Equation (5) was numerically solved by using an alternating direct implicit (ADI) method, which is unconditionally stable, irrespective of the time step, Δt, employed.

The two dimensional square calculation area of 750×750 grids for the phase-field and solute field and that of 75×75 grids for the thermal field are prepared. The grid sizes of the phase-field and the concentration field, and the thermal calculation are 1.0×10^{-8}m and 1.0×10^{-7}m respectively. A small triangle solid of 15×15 grids is initially put in the corner. The equations are solved at different initial temperature fixed on the boundary for the thermal equation. The choice of the Δt must be made in such a way that the equations remain stable under time-step iteration. For the diffusion equation in two dimensions it can be shown that $\Delta t < \Delta x^2/(4D_{\mathrm{L}})$ for stability, So a value of $\Delta t = \Delta x^2/(5D_{\mathrm{L}})$ has been selected in this study. We only calculate the quarter of the dendrite because of the symmetry of the dendrite.

5. Results and discussion

5.1. Dendritic growth

The dendrite shapes of Al–Cu 1.96mol% alloy are shown in Fig.1 at different initial temperatures. The calculated results show that many features are consistent with experience based on observations of dendritic growth in transparent materials and metallographic examination of cast microstructures.

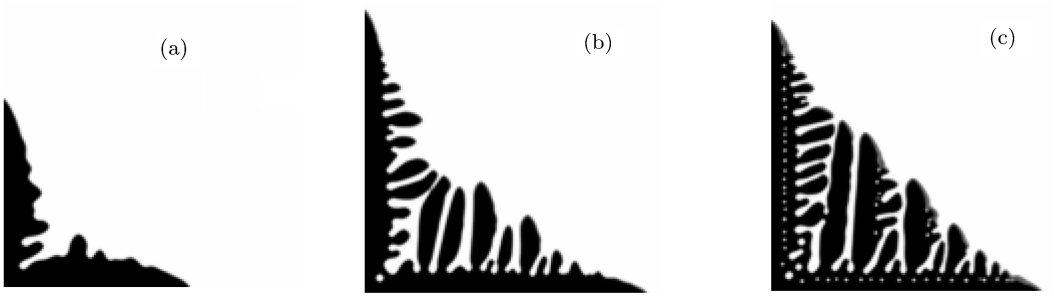


Fig.1. The dendritic shape for Al–Cu 1.96mol% alloy: (a) 906K(0.333ms), (b) 900K(0.173ms), (c) 895K(0.147ms).

In Fig.1(a) the primary dendrite arms growth is slower than the others, and there are no well-developed secondary arms. In Figs.1(b) and 1(c) the dendritic has well-developed secondary arms, and the primary arms become finer. The results indicate that the dendritic has well-developed secondary arms with the increase of undercooling. The competitive growth of the secondary arms during solidification is observed. The tendency of the sidebranches begins their growth in a direction not perpendicular to the primary arm, but later, gradually develops a growth axis that is perpendicular to the primary arm. Behind the dendrite tip, the root of the side arm is significantly narrower than the body of the side arm. These features are commonly observed in real dendrites.

The tip speed, radius and the solute Peclet number as a function of temperature are plotted in Figs.2 and 3 respectively. The results indicate that the solute Peclet number and the tip speed decreases with the increase of temperature, but the tip radius increases. The result of the Peclet number agrees well with Ivantsov theory.

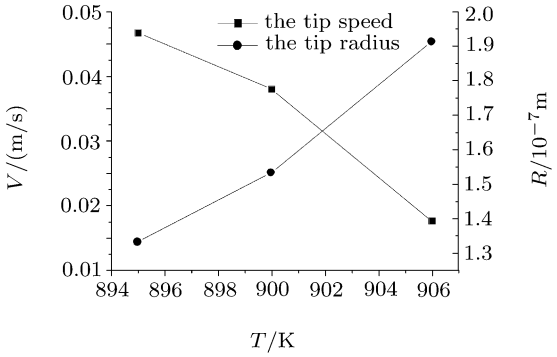


Fig.2. The tip speed and radius versus initial temperature.

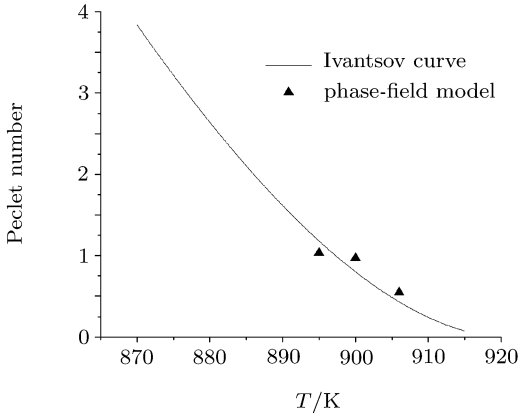


Fig.3. The Peclet number versus temperature.

5.2. Solute segregation patterns

The solute patterns for Al–Cu 1.96mol% alloy dendritic growth at the different initial temperature are shown in Fig.4. The results show that the concentration profiles agree well with the dendrite growth.

The spine of the primary arm has a low concentration, and the mushy regions between the dendrite secondary arms have the highest concentration. The spines of low concentration on the secondary arms are as low as the spines of the primary arms. The increased undercooling is known to increase the severity of microsegregation and this is shown nicely in the calculated pattern. The increase of initial temperature reduces the highest concentration of dendrite. The solute gradients form in the solid/liquid interface regions since the solute diffusivity is much less than the speed of the boundary transition. The solute gradients existing in the interface before the dendrite tip are the highest because the tip speed is the fastest.

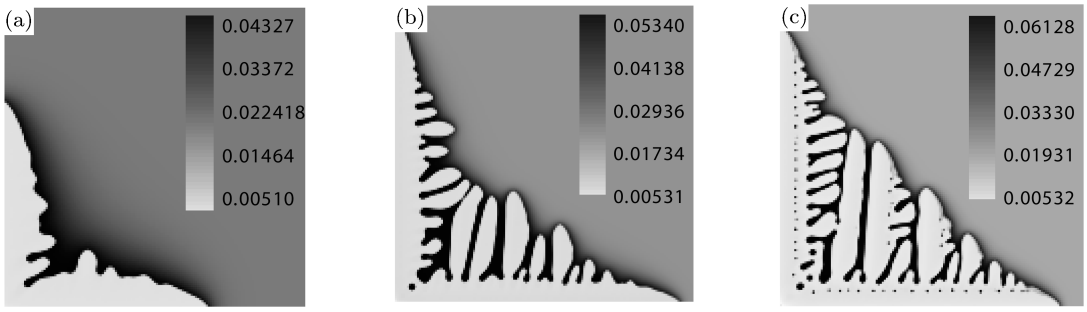
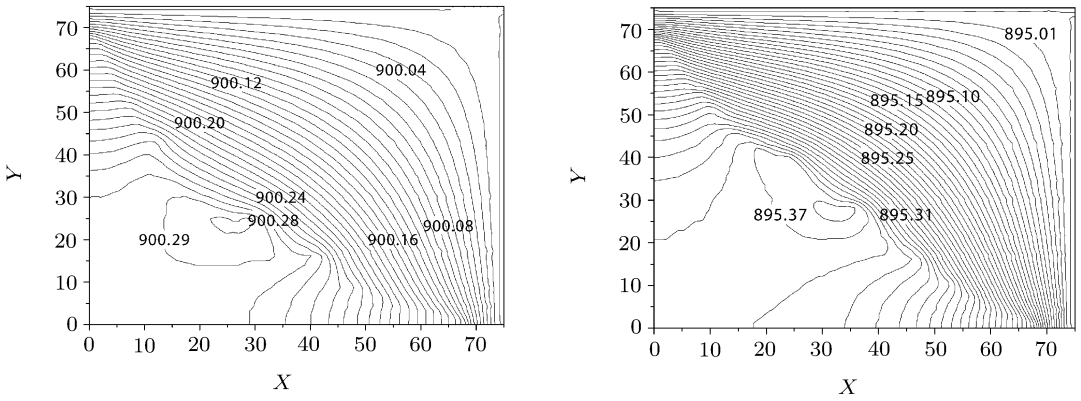


Fig.4. The concentration profiles for Al–Cu 1.96mol% alloy: (a) 906K(0.333ms), (b) 900K(0.173ms), (c) 895K(0.147ms).

5.3. Temperature field

Figure 5 shows the contour line of the temperature field at two different undercooling conditions. All curves show the location of the hottest point during the dentritic growth, that corresponds to the tips of those secondary arms which grow towards each other and form a closed liquid pocket. Melt in this pocket is of the highest temperature due to the release of the latent heat by these growing secondary arms. The local peaks occur when two or more side-branches growing towards each other merge, stop growing and consequently produce the latent heat. The tips are the coldest parts of the dendrite.

The temperature gradient in the solid/liquid interface is greater than that at other places, and the biggest temperature gradient lies in the tips. The change of the temperature gradient is owing to the release of latent heat in the dendritic growth. The lower the initial temperature is, the larger the temperature gradient in the solid/liquid interface is. This is because the decrease of initial temperature increases the velocity of dendritic growth and the release of latent heat.



(a) 900K (0.173ms) (b) 895K (0.147ms)

Fig.5. The temperature field for dendrite growth at different undercooling conditions.

6. Conclusion

(1) The dendrite growing morphologies could be simulated by linking the phase-field method to CALPHAD realistically, and the dendritic has well-developed secondary arms with the increase of undercooling temperature. The results of simulation agree well with the features commonly observed in real solidification of binary alloy.

(2) The solute Peclet number and the tip speed decrease with the increase of temperature, but the tip radius increases. The computed value of Peclet number agrees well with the Ivantsov solution.

(3) The spine of the primary arm has a low concentration, and the mushy regions between the dendrite secondary arms have the highest concentration. the solute gradients existing in the interface before the dendrite tip are the highest. The increase of initial temperature reduces the highest concentration of dendrite.

(4) The heat gradient in the solid/liquid interface is greater than that at other places, and the highest heat gradient lies in the tips. The lower the initial temperature is, the higher the heat gradient is.

References

[1] Wheeler A A, Murray B T and Schaefer R J 1993 *Physica* D **66** 243

[2] Yu Y M, Yang G C, Zhao D W, Lü Y L, Karma A and Beckermann C 2001 *Acta Phys. Sin.* **50** 2423 (in Chinese)

[3] Zhao D P, Jing T and Liu B Ch 2003 *Acta Phys. Sin.* **52** 1737 (in Chinese)

[4] Li M E, Yang G C and Zhou Y H 2005 *Acta Phys. Sin.* **54** 454 (in Chinese)

[5] Wheeler A A, Boettinger W J and McFadden G B 1992 *Phys. Rev.* A **45** 7424

[6] Murray B T, Wheeler A A and Glicksman M E 1995 *J. Crystal Growth* **154** 386

[7] Kim S G, Kim W T and Suzuki T 1999 *Phys. Rev.* E **60** 7186

[8] Suzuki T, Ode M, Kim S G and Kim W T 2002 *J. Crystal Growth* **237–239** 125

[9] Long W Y, Cai Q Zh, Chen L L and Wei B K 2004 *Trans. Nonferrous Met. Soc. China* **14** 291

[10] Yu Y M, Yang G C, Zhao D W and Lü Y L 2003 *Chin. Phys.* **12** 211

[11] Long W Y, Cai Q Zh, Chen L L and Wei B K 2005 *Acta Phys. Sin.* **54** 256 (in Chinese)

[12] Li M E, Yang G C and Zhou Y H 2005 *Chin. Phys.* **14** 838

[13] Long W Y, Cai Q Zh, Wei B K and Chen L L 2006 *Acta Phys. Sin.* **55** 1341 (in Chinese)

[14] Long W Y, Cai Q Zh, Chen L L and Wei B K 2005 *Foundry* **54** 1097 (in Chinese)

[15] Zhu J Z, Liu Z K, Vaithyanathan V and Chen L Q 2002 *Scripta Mater.* **46** 401

[16] Chao J and Liu Z K 2003 *Acta Mater.* **51** 4447

[17] Dinsdale A T 1991 *CALPHAD* **15** 317

[18] Andersson J O, Helander T, Höglund L, Shi P F and Sundman B 2002 *CALPHAD* **26** 273